

Additive manufacturing of alumina-silica reinforced Ti6Al4V for articulating surfaces of load-bearing implants

Bryan Heer, Yanning Zhang, and Amit Bandyopadhyay*

W. M. Keck Biomedical Materials Research Lab

School of Mechanical and Materials Engineering

Washington State University

Pullman, WA 99164-2920, USA.

*E-mail: amitband@wsu.edu

Abstract

In this study, functional gradation via layer-wise additive manufacturing was coupled with Al₂O₃ and SiO₂ ceramics' advantages to creating a composite of Ti6Al4V (Ti64) with improved hardness and wear resistance. It was hypothesized that with the addition of Al₂O₃ and SiO₂ into Ti64, wear-resistance and hardness would increase when compared to the base Ti64 alloy. It was also hypothesized that if the structure could be created, an additional laser pass (LP) over the structure's top surface would further increase the hardness. Successfully fabricated composite structures were found to have varying phases of TiSi₂ and Ti₅Si₃. Refined α -Ti grains were present in the composite region. The interface between the composite and pure Ti64 regions was crack-free, indicating a metallurgically sound bond. Dendritic microstructures were observed with the addition of LP on the composite top surface. Hardness was increased from 323.8 ± 9.6 HV in Ti64 substrate to 434.7 ± 7.3 HV and 677.1 ± 29.7 HV in 3D Printed Ti64 and the composite sample, respectively. An LP increased hardness further to 938.8 ± 57.5 HV, a 186% increase in hardness than the original Ti64 alloy. Wear resistance was also increased with

the addition of Al₂O₃ and SiO₂ by ~90%, indicating the potential processing variations placed on this material system to produce structures with site-specific functionality for biomedical applications, particularly in articulating surfaces of load-bearing implants.

Keywords: Al₂O₃, SiO₂; Ti6Al4V; additive manufacturing; wear resistance; Implants.

1.0 Introduction

Load-bearing implants such as total hip arthroplasty (THA) and total knee arthroplasty (TKA) are used for many patients every year. Typically, Cobalt-Chromium-Molybdenum (CoCrMo) alloy is utilized as the choice material due to its high wear and corrosion resistance¹. This material is widely used in articulating surfaces in the load-bearing device, such as the femoral head on a hip implant, where the most significant wear occurs. Unfortunately, patients over the years have shown an increased risk of leukemic cancer and lymphomas associated with Co and Cr ion release during wear and biocorrosion on the implant surfaces²⁻⁴. Increased Co toxicity levels in the human body can also increase various neurological and cardiological symptoms⁴.

Furthermore, hip implants are typically constructed with the CoCrMo femoral head on a Ti64 stem to reduce the implant's weight for patient functionality. However, the two materials joined together at the implant neck have allowed for taper corrosion to occur and are now identified as a standard THA failure mode⁵⁻⁹. This corrosion pathway has caused the implant's loosening with the need for revision surgeries and unnecessary patient trauma for multiple cases.

With complications like these, significant research efforts are being pursued in recent years to mitigate these issues¹⁰⁻¹⁴.

It has been suggested by replacing Co-based materials with Ti64 to eliminate Co and Cr ion toxicity and prevent bio-corrosion at the implant's taper. However, pure Ti64 alloy has low wear resistance. After a while, the debris dropped from the worn Ti64 surface could still damage the tissue. The deposition of ceramic coating on Ti64 alloy is hypothesized to improve the wear resistance and prevent metal ion leaching. Alumina and alumina-based composites have been deemed suitable for these types of applications, as excellent chemical stability reduces the chance of cytotoxic ion release from corrosion in articulating surfaces¹⁵. In recent years, success with fabricating alumina-based ceramics has been shown with laser-based additive processes. Studies have primarily focused on ceramic's processability instead of mechanical properties¹⁶⁻²¹. Still, with ceramic coated THA, new issues begin to surface (**Figure 1a-i**), such as interfacial fracture, cup loosening due to bio-tribocorrosion, and mal-positioning²². Long-term data does not exist for these alternatives. Naturally, the system's lasting viability is still mostly unknown.

Silica (SiO_2), when combined with Al_2O_3 in a 3:2 ratio, forms mullite, which is one of the most commonly used ceramic phases in traditional and advanced ceramics²³. Under laser-based processing conditions, SiO_2 can dissociate and react with the matrix material in a composite system. SiO_2 addition onto Ti64 has shown this reaction through the formation of Ti_5Si_3 and significantly increased the wear resistance of Ti64 by up to 98%²⁴. Moreover, researchers have proved that SiO_2 -based tribofilm with anti-friction behavior could be formed on the SiO_2 doped composite matrices (polymer/ SiO_2 and metal/ SiO_2) under wear testing conditions^{25,26}. With the multitude of advantages Al_2O_3 and SiO_2 hold by themselves, introducing these oxide-based ceramics as a reinforcement phase in a Ti64 matrix could show considerable improvements in

mechanical properties for load-bearing articulating surfaces in a biomedical application (**Figure 1a-ii**).

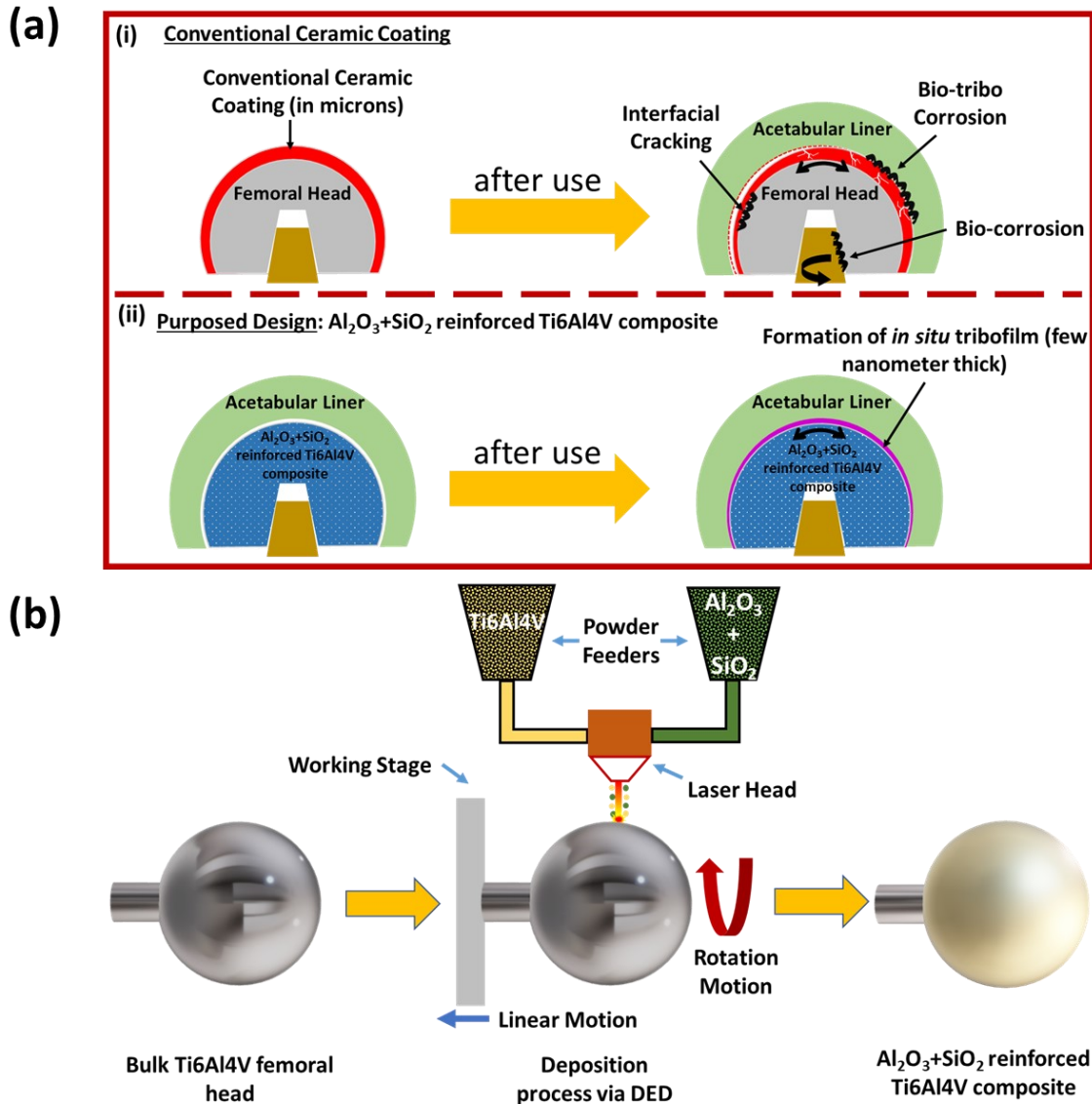


Figure 1: (a) Illustration of the disadvantages of current conventional ceramic coating on the femoral head and the advantage of proposed ceramic coating on the femoral head. (b) Schematic of the deposition process on a bulk Ti6Al4V femoral head via the DED technique.

Although the deposition of ceramic reinforced metal composite on the surface of a metallic material could be achieved by traditional methods such as physical vapor deposition

(PVD) and chemical vapor deposition (CVD), both time and economy of using these methods to make the deposition are very high. Current laser-based additive manufacturing technology has shown its feasibility of fabricating both metallic and ceramic materials. Compared to the traditional methods, using additive manufacturing techniques to deposit ceramic and metallic composite on a metallic substrate is much more efficient due to high customization. By taking the advantages of additive manufacturing, researchers have investigated additive manufactured Ti64 with multiple reinforcement phases to understand how a second phase can influence the material's working life under wearing conditions^{27,28}. For example, TiB/TiC + Ti64 composite coatings were realized through laser processing and significantly increased the wear resistance of Ti64²⁹, while TiC/Ti64 composites reduced wear volume loss up to ~70% compared to pure Ti64³⁰. Furthermore, researchers have explored the wear behaviors with the addition of the TiC phase²⁹⁻³³ TiN phase³⁴ and SiC phase³⁵ into Ti alloys via laser processing. While these studies primarily investigated the properties of the single material, taking those properties and incorporating them into the design by manufacturing entire systems with these improvements only where necessary is essential for advancing medical device fabrication.

However, understanding these ceramic-based regions' processability is a different issue as the required build parameters for ceramics and metals in a laser-based manufacturing system are mostly different. A separate set of challenges arises if the deposited structure is purely a metal/ceramic composite or if the deposited structure is gradually transitioning from metal into a metal/ceramic composite to create a functionally graded material. In the latter case, build parameters change to build height and require tight-monitored processing controls. However, suppose a coherent structure is made with a ceramic-reinforcement phase. In that case, the results

typically show a significant increase in mechanical properties like hardness and wear resistance compared to the unreinforced metal.

In this study, Al_2O_3 and SiO_2 materials were dynamically added into Ti64 alloy via directed energy deposition additive manufacturing, and the resulting mechanical and material properties were explored. Significant processing optimization was needed to manufacture crack-free parts with the ceramic reinforcement phase, a common defect in processing ceramics through laser-based additive manufacturing. Microstructures, phases, microhardness, elemental analysis, and tribological characterizations were completed on the samples, and hard, highly wear-resistant structures were realized. It is envisioned that this study will impact load-bearing articulating surfaces in the biomedical field as we show how a gradually changing structure from Ti64 to ceramic-reinforced Ti64 can add functionality where desired in a way only possible through advanced additive manufacturing (**Figure 1b**).

2.0 Materials and Methods

2.1 Laser engineered net shaping (LENSTM) processing

LENSTM processing is a directed energy deposition (DED)-based additive manufacturing or additive manufacturing (AM) method which takes feedstock material in powdered form and produces a freestanding, near net shape part. The technology works by flowing metallic or ceramic powder through powder feeders on the system's side into the focal point of an Nd:YAG laser, which rapidly melts and solidifies the powder onto an interchangeable metal plate substrate. The substrate is located on a stage that moves in the X-Y plane, and its movement is determined by the tool path created from the slice file of the user's computer-aided design (CAD) file. Once a single layer is deposited onto the substrate, the deposition head translates in the Z

direction at a specified slice height, and the next layer begins to form on top of the first. This process is continued until the CAD file comes to life in a near-net shape part on the substrate. The part is made in a sealed, oxygen-controlled environment purged with inert argon gas to eliminate oxidation during the rapid melt and solidification process. As the LENSTM system has multiple powder feeders, multiple powder types can be placed into separate powder hoppers, allowing materials to change instantly during the build process. This feature makes LENSTM-processing ideal for creating metal-ceramic composites via laser-based additive manufacturing and was utilized in the study.

Samples were fabricated using a LENSTM-750 (Optomec Inc., Albuquerque, NM) system. **Figure 2** demonstrates the schematic of the LENSTM processing. Specifically, Ti64 powder (ATI Powder Metals, PA, US) was loaded into powder feeder 2, and a mixture of 72%-28% Al₂O₃ (AL-604, Atlantic Equipment Engineers, Bergenfield, NJ)-SiO₂ (silica micro pearl powder, Industrial Powder, Buffalo Grove, IL) was loaded into powder feeder 1. Powders were mechanically sieved to a 45-145μm particle size distribution before deposition onto the 3mm thick Ti64 substrate. Samples included LENSTM-deposited Ti64, Ti64 transitioning to Al₂O₃/SiO₂-Ti64 composite (Ti64+C), and Ti64 transitioning to Al₂O₃/SiO₂-Ti64 composite with the addition of a laser-pass (LP) on the topmost surface of the build (Ti64+C+LP). Transitioning between the two powders was accomplished by dynamically increasing the powder flow rate of powder feeder 1 while maintaining the powder feeder 2 powder flow rate the same. An LP was accomplished by stopping powder flow on the top layer and running the laser over the pre-deposited surface. The specific processing parameters can be found in **Table 1**, the starting point for the initial Ti64 deposit.

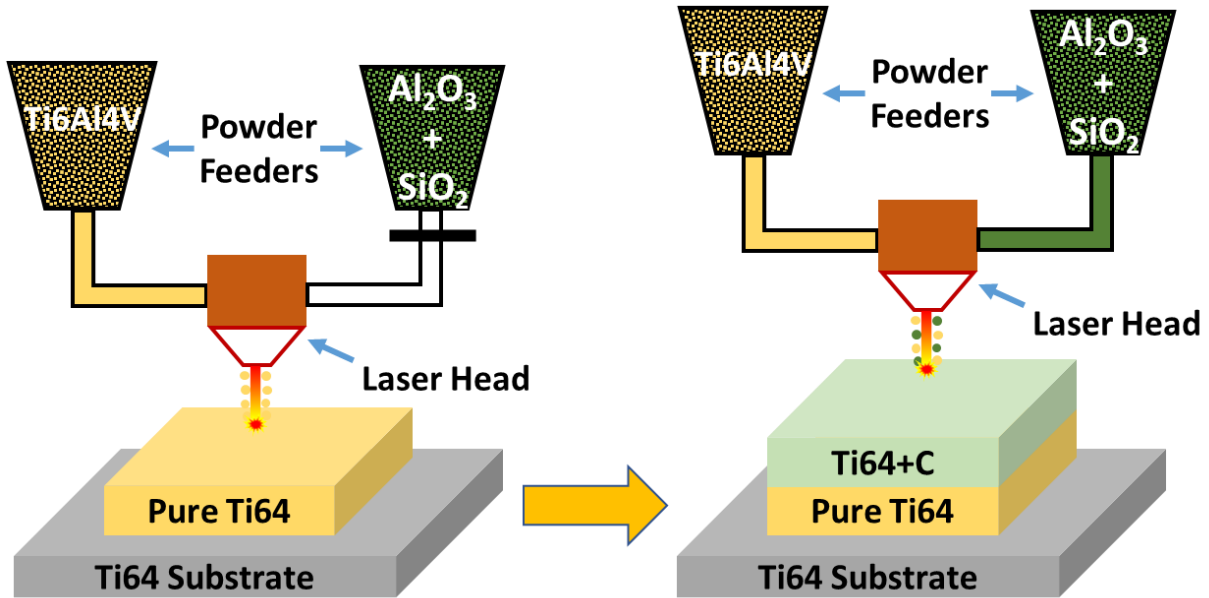


Figure 2: Schematic of the deposition process of Ti64+C on Ti6Al4V via the DED technique.

Table 1: LENSTM-processing parameters for successful Ti64 and Ti64+C deposition.

Sample	Power (W)	Hatch spacing (in)	Powder feed rate (g/min)	Slice thickness (in)	Hatch/contour speed (in/min)	Oxygen level (ppm)
Ti64	440	0.022	~20	0.008	~20	<20
Ti64+C	400	0.022	PF1: ~20 PF2: ~10	0.008	~20	<20

2.2 Characterization

Samples were cut along their cross-sections to expose how features changed along with the build height. Cross-sections and top surfaces were mechanically ground from 120-2000 grit sandpaper through standard wet grinding, followed by polishing with alumina deionized water suspensions from 1-0.05 μ m. Samples were then cleaned in an ultrasonic bath in 100% ethanol for 15 minutes to remove any residual alumina particles. Cross-sections were etched with Kroll's

reagent (92 mL DI water, 2 mL HF and 6 mL HNO₃) to expose microstructural features.

Microstructures and elemental maps were viewed using a field emission scanning electron microscope (FESEM, FEI-SIRION, Portland, OR). Phase analysis was completed via XRD (X'Pert Powder, PANalytical Inc., Westborough, MA) from 20-80 2 θ ° with a Cu-K α (λ = 0.15406nm) source. A Vickers microhardness indenter (Phase II Model 900-391, Upper Saddle River, NJ) was used to measure hardness variations on the samples' top surfaces to compare the ceramic's hardness loaded regions. Tribology using a bio-tribometer (Ducom, Bangalore, India) was completed on the samples' top polished surfaces. A 5N load was applied to the sample on a linearly-reciprocating stage that traversed a 10mm amplitude at 1200 mm/min. The sample was submerged in room temperature DI water, and a 3mm diameter tungsten carbide (WC) wear ball was used for its high hardness and electrical conductivity to allow contact resistance measurements to be made during the test. Tribology tests followed a linearly reciprocating ball-on-flat sliding wear model according to ASTM standard G133-05³⁶.

3.0 Results

Microstructures and elemental mapping

Microstructural features were investigated along the build's cross-section to observe how processing changes and material addition influenced grain size and morphology. As shown in **Figure 3**, microstructures were altered when transitioning from the Ti64 region to the Ti64+C region. In **Figure 3c**, typical acicular α -Ti grain structures surrounded by pre-existing β -Ti grain boundaries were evident in the Ti64 region. Moving upwards in the build direction to the interface where Al₂O₃/SiO₂ began to be dynamically added to the melt, **Figure 3b**, a noticeable grain size reduction was observed in the Ti64+C region compared to the Ti64 deposit. The plate-like α -Ti microstructure is evident in this Ti64+C region, as shown in **Figures 3b** and **c**.

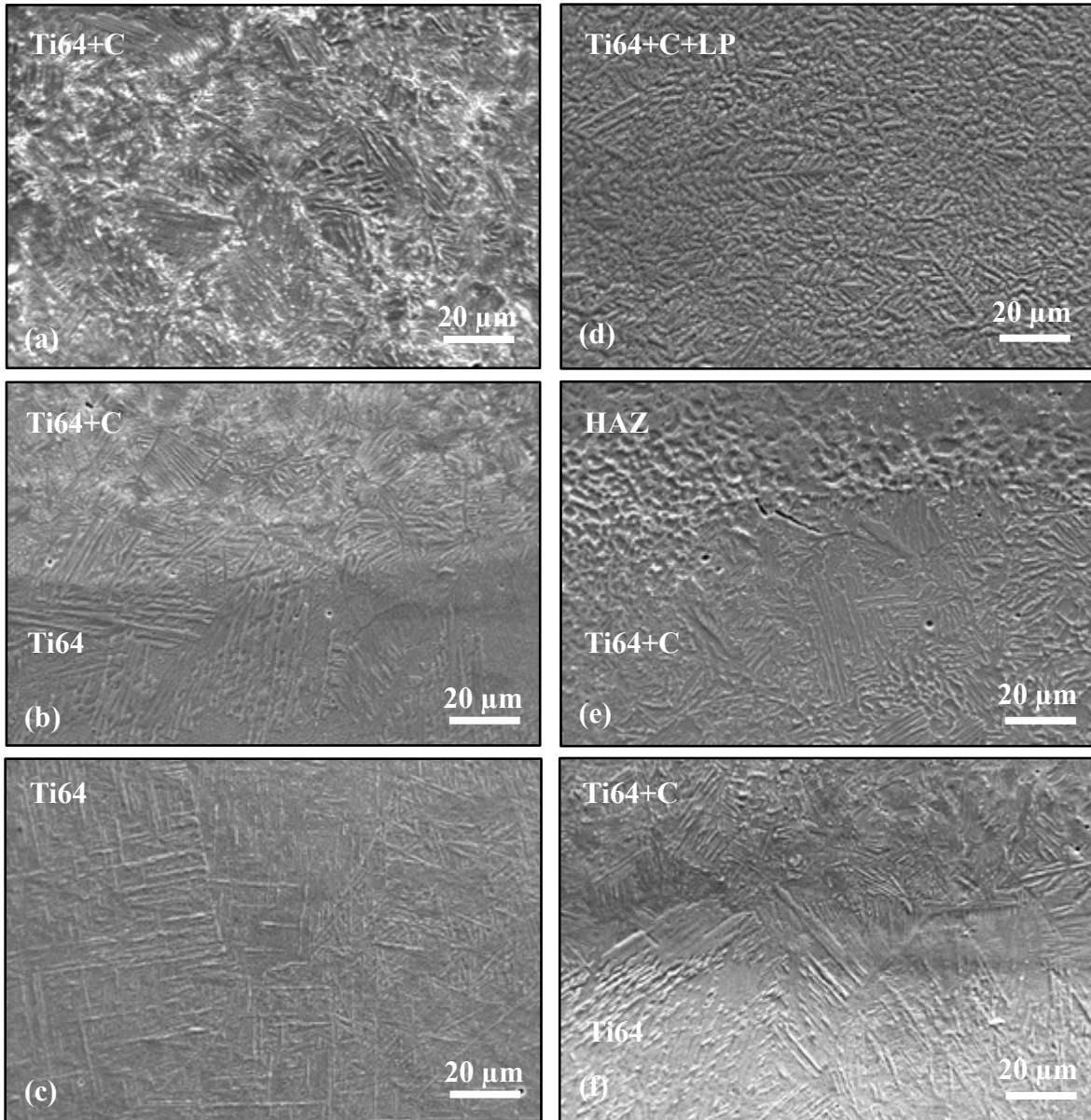


Figure 3: Microstructures of (a) Ti64+C, (b) interface of Ti64+C and Ti64, and (c) Ti64. Microstructures of the HAZ of (d) Ti64+C+LP, (e) interface of HAZ and Ti64+C, and (f) interface of Ti64+C and Ti64 in the laser pass sample.

With the addition of a laser pass, the top surface of the Ti64+C+LP structure showed evidence of a dendritic microstructure with an extremely refined morphology compared to the Ti64+C with no laser pass region. This specific morphology is shown in **Figure 3d**. With the addition of a laser pass, a prominent heat-affected zone (HAZ) interface was observed within the Ti64+C and

is shown in **Figure 3e**. Directly below the HAZ, microstructures consisted of α -Ti lathes and morphology similar to the Ti64+C regions in **Figure 3e** and **Figure 3f**, indicating that the LP was effective as solely a surface modification. The LP addition showed evidence of cracking and can be seen in **Figure 3e** at the HAZ interface. EDS was utilized to generate elemental maps across the Ti64 and Ti64+C interface to verify an increase in aluminum and silicon content in the Ti64+C region from the addition of Al_2O_3 and SiO_2 . As shown in **Figure 4**, as Ti64 transitioned into Ti64+C, aluminum and silicon maps increased in intensity, validating the addition of Al_2O_3 and SiO_2 into the composite structure.

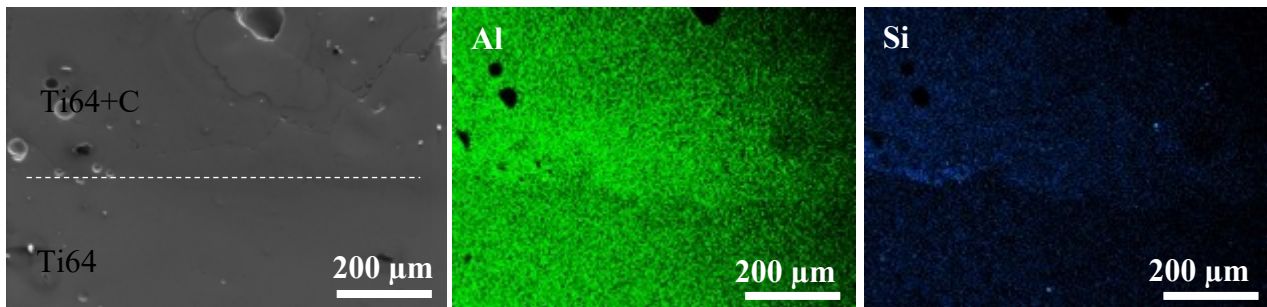


Figure 4: Elemental dot maps of aluminum and silicon at the Ti64+C and Ti64 interface.

Phase analysis

Phase analysis using x-ray diffraction (XRD) was completed, and the analyzed spectra are presented in **Figure 5**. The 100% ceramic deposit, which consisted of the 72%-28% $\text{Al}_2\text{O}_3/\text{SiO}_2$ premixed composition, showed an amorphous phase, a corundum phase (PDF# 10-0173), and an aluminum-rich mullite compound $\text{Al}_{5.65}\text{Si}_{0.35}\text{O}_{9.175}$ (PDF# 82-1237) for the best fitting peaks. Examining the Ti64+C structure, which had the same ceramic composition but at a lower concentration, mullite or corundum peaks were not observed. Instead, various forms of titanium silicides were observed with the Ti64+C sample having a small percentage of TiSi_2 (PDF# 35-0785) and the addition of a laser pass in the Ti64+C+LP sample showing Ti_5Si_3 phase

(PDF# 29-1362) alongside titanium phase (PDF# 44-1294). **Figure 6** shows another EDS elemental map at a dendritic region in the Ti64+C+LP sample, showing aluminum and silicon-rich precipitate phases along the grain boundaries. Furthermore, compared to the spectra of the LENSTM-processed Ti64, apparent peak broadening was observed on the characteristic (101) peak in the Ti64+C+LP condition, pointing to excess residual strain accumulation. It should be reminded here that the addition of a laser pass cracked the top surface of the structure and limited the breadth of mechanical testing for this condition.

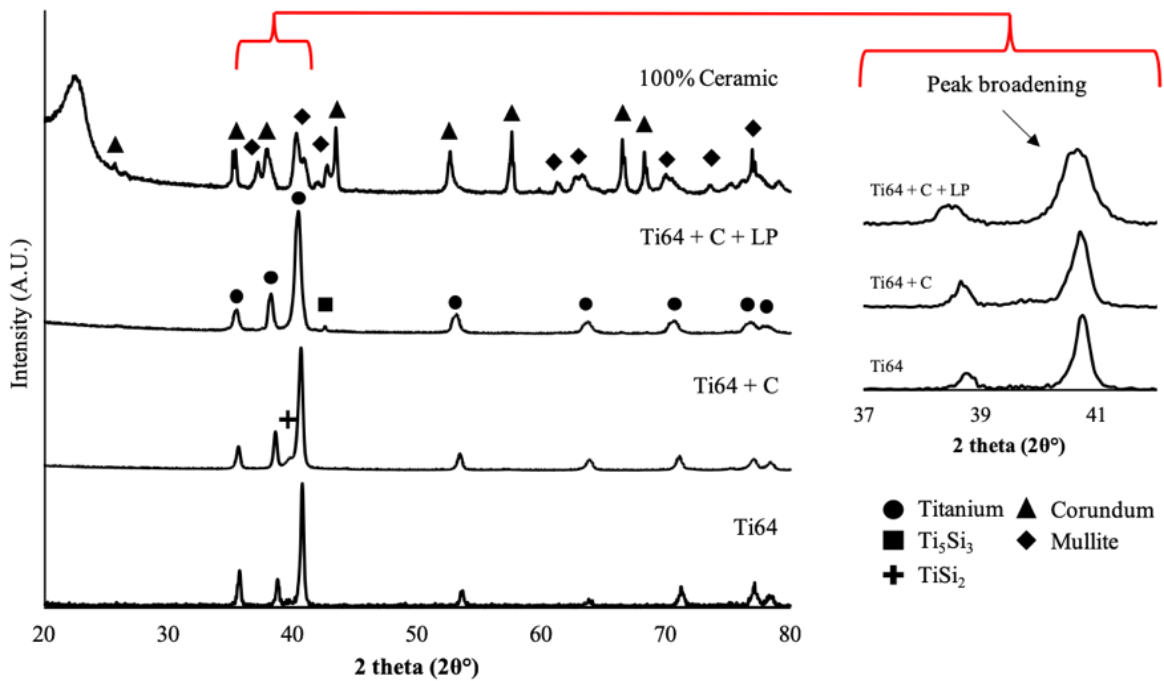


Figure 5: XRD spectra ($\lambda = 0.15406\text{nm}$) of LENSTM-processed Ti64, Ti64 with ceramic reinforcement, the same composition with a laser pass, and pure LENSTM-processed ceramic. Peak broadening effect with the addition of laser pass is also shown.

Vickers microhardness

Hardness measurements were taken over six separate indentation locations and were averaged to obtain a final surface hardness. On the topmost surface of the build, hardness measurement was done, and extreme care was taken to polish only the minimum material to

ensure any effects from the laser pass were not mitigated. Hardness results are shown in **Figure 7**. The Ti64 substrate measured 323.8 ± 9.6 HV hardness, which was improved to 434.7 ± 7.3 HV in LENSTM-processed Ti64. With the addition of Al₂O₃ and SiO₂, Ti64+C hardness increased by 109% to 677.1 ± 29.7 HV, which increased even further by 186% to 938.8 ± 57.5 HV in Ti64+C+LP compared to the commercially processed Ti64 substrate. 100% of the Al₂O₃/SiO₂ mixture was deposited onto a different Ti64+C sample to investigate pure ceramic's processability. While deposition was successful, large amounts of cracking ensued characterization past hardness was deemed unreasonable. Nevertheless, this 100% mixture showed a large increase of over 300% to 1337.8 ± 48.3 HV, demonstrating the possibilities of an extremely hard ceramic composite coating through further processing optimization.

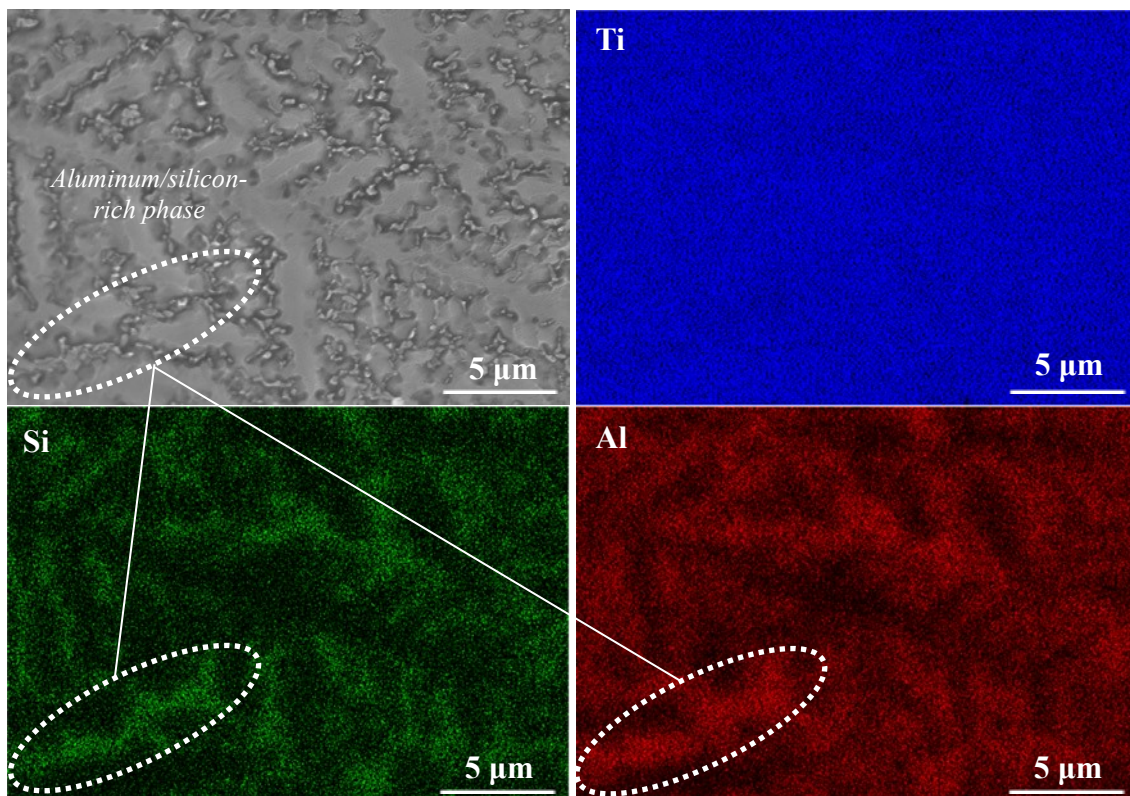


Figure 6: EDS dot map along dendrite feature in the Ti64+C+LP sample showing evidence of an aluminum/silicon rich precipitate phase.

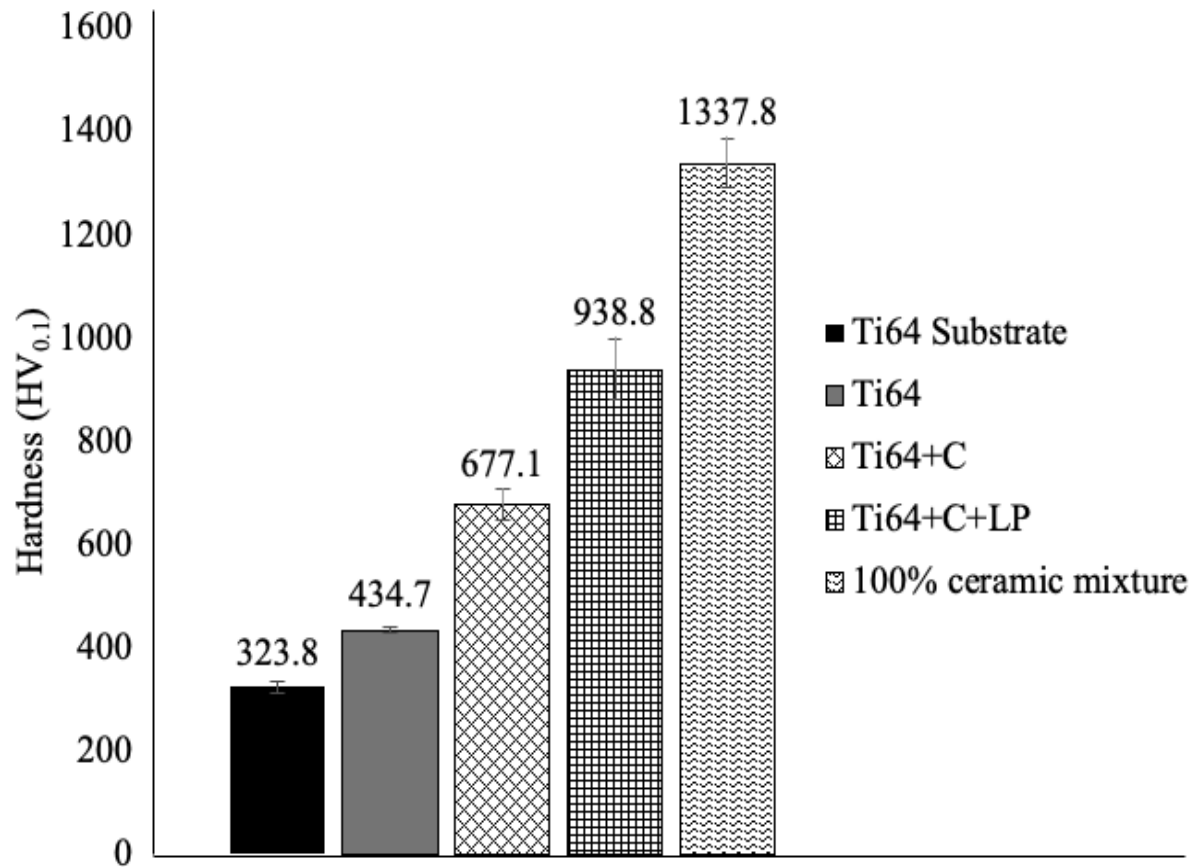


Figure 7: Top surface microhardness plot comparing build conditions to the conventionally processed Ti64 plate.

Tribology

To further characterize the effect of Al₂O₃ and SiO₂ addition into Ti64, wear studies were completed on Ti64 and Ti64+C and compared to a commercially rolled Ti64 plate. Multiple wear runs were completed on the same surfaces in which hardness was completed, and the average wear volume was calculated and reported. Furthermore, dynamic changes in overall compound wear (vertical wear ball Z-displacement during the test) and contact resistance between the worn ball and tribosurface have been reported. Investigating the wear track on the commercially processed Ti64 alloy exposed a large amount of plastic deformation accumulation

on the ends of the wear track and along the wear track's sides, as seen in **Figure 8a**. A higher magnification image of the wear track showed evidence of an extensive plowing characteristic of Ti64 materials under loaded articulating conditions from plastic deformation forming grooves on the tribosurface. The same Ti64 alloy, the amount of plastic deformation, and grooving were less prevalent by laser processing than commercially processed material (**Figure 8b**). In the Ti64+C sample, plastic deformation was largely reduced with no plastic deformation built upon any wear track region and minimal grooving effects observed at the higher magnification (**Figure 8c**).

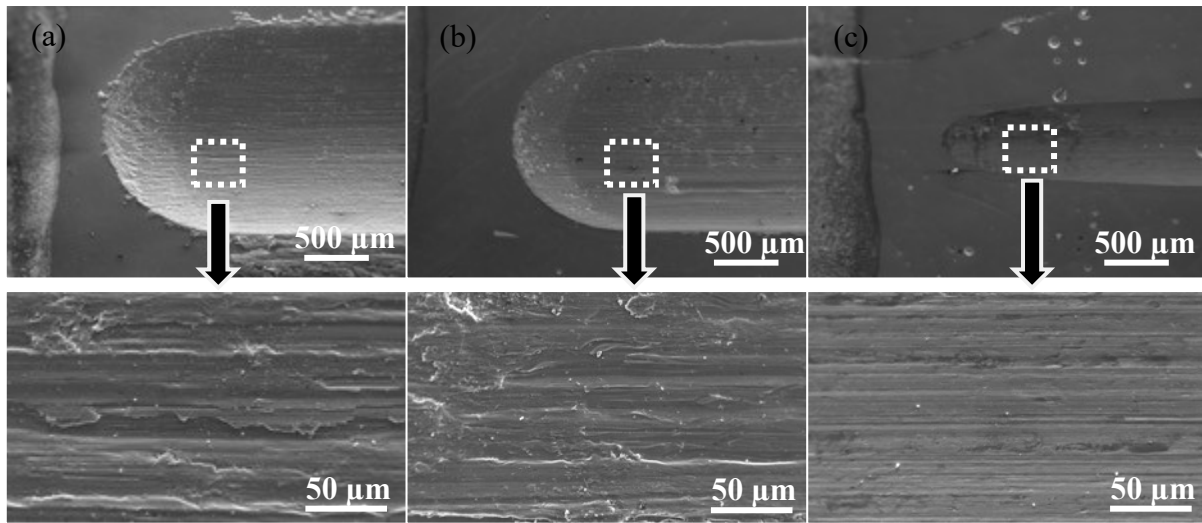


Figure 8: Wear track comparisons between (a) Ti64 substrate, (b) LENSTM-deposited Ti64, and (c) Ti64+C samples.

Commercially processed Ti64 displayed the highest overall wear volume at 2.66 ± 0.06 mm³. Overall, the wear volume of the LENSTM-processed Ti64 was reduced by ~22% to 2.07 ± 0.02 mm³ and reduced even further in Ti64+C by 89% to 0.29 ± 0.01 mm³. In the Ti64+C sample, a steady-state wear regime was quickly established, and wear rates became relatively constant at only 25m into the 1000m test. This result contrasted with the other two conditions with no ceramic phase where wear plateau didn't reach ~600-700m. The contact resistance of the

Ti64+C sample registered at a higher ohm reading (~50-60) compared to both commercially processed and LENSTM-processed Ti64, which maintained a contact resistance of ~6 ohm throughout the entirety of the test. Contact resistance for the Ti64+C sample sharply increased at the beginning of the test from ~25 ohms on the pre-worn surface to ~65 ohm until 25m, where the contact resistance then began to settle around 55 ohms for the remainder of the test. This increase in contact resistance likely indicated a rapid ceramic tribofilm evolution, where once formed and stabilized aided in keeping steady-state wear. Average coefficients of friction for the Ti64 substrate, Ti64, and Ti64+C samples were 0.34 ± 0.01 , 0.32 ± 0.02 , and 0.50 ± 0.01 , respectively.

4.0 Discussion

Microstructures and hardness: Laser deposition processes of metals, such as LENSTM, can have refined metastable microstructures compared to conventional processing due to rapid solidification rates²⁴. These fine microstructural features can directly influence the final material's mechanical properties and typically have higher hardness over their conventionally processed counterparts. In Ti64, with phase amounts dependent on cooling rates, complex microstructural zones of mixed phases are usually found spread out across the bulk of the structure³⁷⁻⁴⁰. Martensitic acicular α -Ti grain structures are typically found in laser processed Ti64 and were evident in this study. As the temperature of the melt pool is rapidly cooled, the β -Ti phase first forms from the liquid and then transforms to α -Ti, leaving a microstructure of α -Ti surrounded by prior β -Ti grain boundaries^{37,41}. With the fast cooling of LENSTM, the initial α -Ti phase is of an acicular or "needle-like" morphology and can change with previous layers' partial remelting⁴². Partial remelting of previous layers occurs from the successive layers deposited on

top of each other subjected to thermal cycling and can provide enough thermal energy to remelt and solidify the structure along the same process as stated above. After multiple layers, this thermal energy is less significant to prior layers. Remelting does not occur; therefore, multiple solid-state transformation cycles from leftover β -Ti to the α -Ti phase occur^{37,39,40}. Particularly in the Ti64+C region, repetitive thermal cycles from successive layers increased the residual temperatures in the deposited structure and were heightened from the addition of the ceramic phase, which inherently retains heat from their insulative nature. Therefore, this repetitive thermal cycling, coupled with a ceramic phase, likely caused the acicular α -Ti (**Figure 3c**) to grow and appear more like plate-like α -Ti (**Figure 3a**).

Compared to the substrate, LENSTM-deposited Ti64 (Ti64) increased in hardness by 34%. This was due to the rapid solidification of the laser processing quenching the material and creating the harder, martensitic α -Ti phase. Hardness increases of the same material laser processed compared to conventionally processed plates have been widely reported with this rationale. As the amount of ceramic phase increased, hardness also increased. This was partially from the addition of Al₂O₃ into the melt stabilizing the harder hexagonal close-packed α -Ti phase, as aluminum is an α -phase stabilizer for titanium alloys⁴³. Large amounts of α -Ti platelets observed in the microstructures supported this, as little retention of the β -Ti was observed in the Ti64+C region. Hardness increases were also likely influenced by the formation of hard, intermetallic silicide phases in the melt; this phase development is described below.

Phase: Phase evolution in LENSTM additive manufacturing is often complicated as its rapid solidification rates can retain metastable phases in the as-printed condition. The 100% ceramic mixture deposit showed an amorphous phase represented by an amorphous "hump" at about 25° 2-theta. The pure ceramic also showed the corundum phase from the Al₂O₃ addition

and an aluminum-rich mullite phase. When depositing multiple materials in directed energy deposition systems, the particles' density influences the powder stream's flowability as it enters the laser's focal point. Typically, materials with a lesser density tend to build up less than those which are denser as the argon shielding gas can cause an irregular flow rate to the melt pool. Consequently, the overall structure would have less of the lighter material than desired, which was the hypothesized reason an aluminum-rich mullite phase was observed. With SiO₂ having a reduced density compared to Al₂O₃, it is likely that less SiO₂ contributed to the melt than what was designed and caused a silicon-deficient mullite phase to form.

A similar mullite phase was expected to be observed in the Ti64+C and Ti64+C+LP samples, yet no such phase could be resolved. It was thought that when depositing pure ceramic Al₂O₃ and SiO₂, these two materials were the only ones able to react, and the aluminum-silicon mullite compound would form. Conversely, it was hypothesized that in the presence of titanium – Ti64+C and Ti64+C+LP samples – the Al₂O₃ and SiO₂ addition would preferentially react molten titanium and form some form of titanium silicide or titanium aluminide phase, which would account for the lack of mullite phase. This was evident in the XRD spectra with TiSi₂ and Ti₅Si₃ phase retention in the Ti64+C and Ti64+C+LP samples, respectively. While the phase evolution aspect was not heavily investigated in this study, it was thought that TiSi₂ would form first in the Ti64+C sample due to the fast solidification retaining a less-stable titanium silicide phase, and the further thermal energy provided by the laser pass facilitated a favorable reaction to the more stable Ti₅Si₃⁴⁴. Similar reports of a study outlining titanium silicide evolution through combustion synthesis showed the TiSi₂ phase initially formed when combining titanium and silicon powders, and further diffusion advanced TiSi₂ to a more stable Ti₅Si₃ phase⁴⁵. **Figure 6** shows an elemental map of dendritic features in the Ti64+C+LP sample and evidence of an

aluminum/silicon-rich precipitate phase along the dendrite boundary. While no forms of titanium aluminide were identified in XRD, it is possible that some form of alumina-silica phase formation was forming alongside a titanium silicide phase and could not be detected through XRD. As an in-depth phase study was not part of this study's scope, a more significant exploration of the phase evolution occurring in a particular composite system could be completed in future work to understand the complex reactions taking place fully.

Wear characteristics: Characterization of the wear performance of Ti64 composites and how compositional variation affects tribological response has been widely reported^{24,29,30,35,46}. Typically, wear track features and overall wear volume are the only results discussed. In this study, these results and connecting changes in wear kinetics and contact resistance as a sliding distance function are discussed. Wear track features at low and high magnification from this study can be found in **Figure 8**. As commercially processed Ti64 is typically softer than LENSTM-processed Ti64 with the larger fraction of β -Ti, the sample surface has been subjected to large amounts of plastic deformation and adhesion wear during tribological testing. This has been previously reported on Ti64 using the same tungsten carbide ball³⁰. As the Ti64 plastically deforms, wear debris builds up on the tribosurface and begins to act as an abrasive against the two materials in contact, which in turn continually increases the amount of wear and friction until the debris is work hardened. As frictional forces continue to rise, and the wear debris is worked, grooves parallel to the sliding direction are formed, and surface roughness increases³⁰. Plowing describes this phenomenon, and the degree of plowing is proportional to the counter material's hardness⁴⁷. This is why the LENSTM-deposited Ti64, with its slightly higher hardness, exhibited less plowing on the tribosurface and plastic deformation grooves were less prominent. Furthermore, the increase in hardness in the Ti64+C zone reduced these grooves even further.

Average wear track widths also decreased with LENSTM processing and ceramic addition, reducing ~8% from 1.65 ± 0.03 mm on the Ti64 substrate to 1.52 ± 0.06 mm on the LENSTM-processed Ti64 and ~50% 0.81 ± 0.04 mm in the Ti64+C condition.

Compound wear and contact resistance data throughout the first 200m of the test can be found in **Figure 9**. Throughout a tribological test, wear rates can change due to various reasons such as work hardening, increase in asperities across the tribosurface, material build-up, and even chemical reactions forming a tribofilm, which has a different chemical composition, structure, and tribological behavior⁴⁸. Initial "running-in" wear rates are typically heightened compared to final "steady-state" wear rates, and distinguishing these zones is essential for understanding how the system will behave during the work-life of the product⁴⁹. This means that the sooner a material reaches its steady-state wear regime, typically less overall wear is observed on the specimen. As indicated by the vertical dashed line in **Figure 9**, the steady-state wear regime was reached in the Ti64+C sample only ~25m into the 1000m test. For the rest of the ~925m, change in compound wear over sliding distance remained linear. This behavior was mostly different from the other Ti64 conditions, which reached a steady-state wear regime ~600-700m into the test and showed large compound wear increases over the first 600m. An increase in contact resistance over the first ~25m of the test from 25-65 ohm was observed, **Figure 9**, which then stabilized at ~55 ohms for the remainder of the test in the Ti64+C sample. This was likely from a tribofilm formation, where typically, a ceramic layer is formed, which increases the contact resistance. The reason for tribofilm formation can be broken into different groups, and the group of interest is one where the tribofilm is generated from the wear of significant constituents in the sliding surfaces⁴⁸. This is because these are tribofilms typically associated

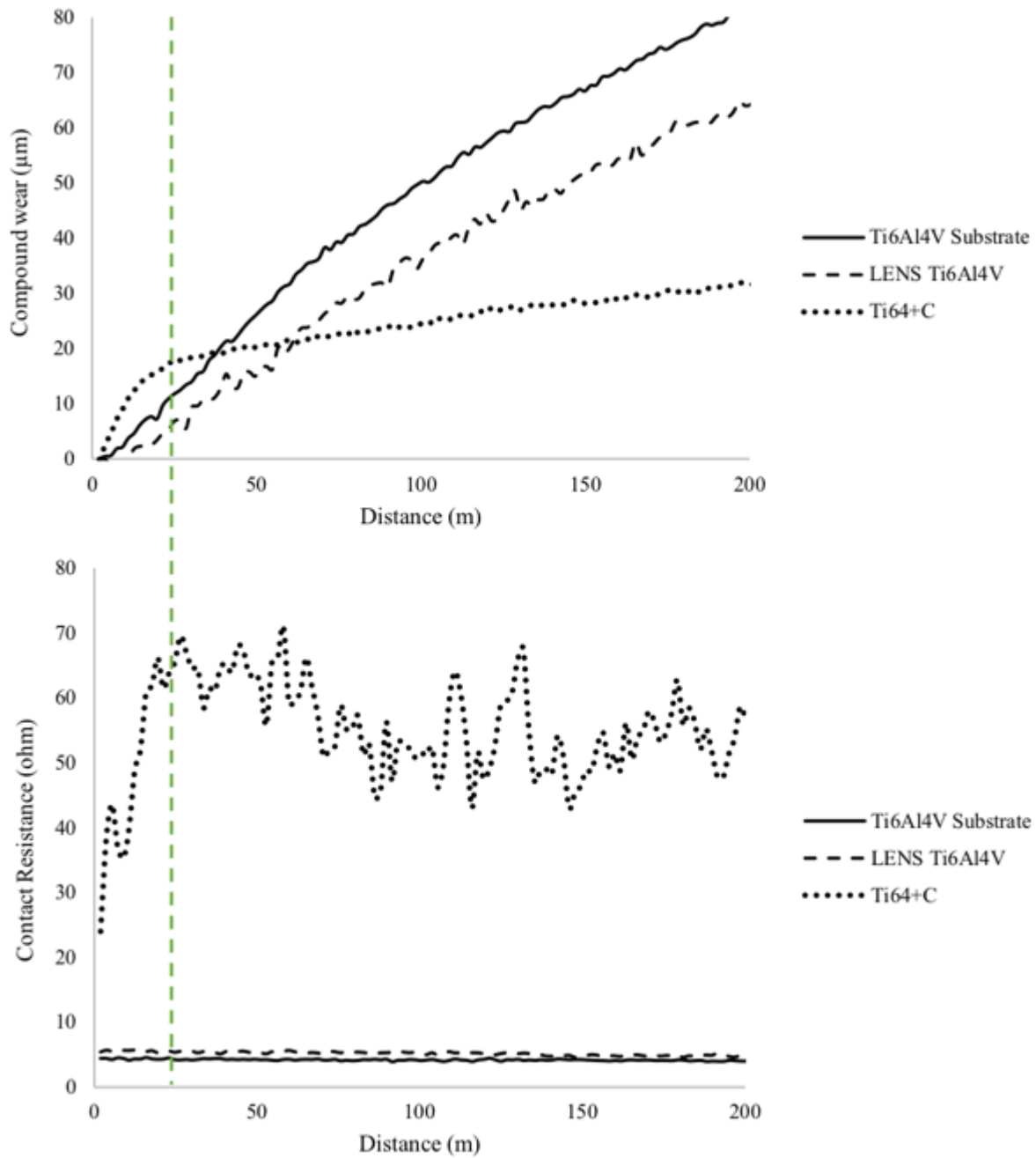


Figure 9: Compound wear (top) vs. contact resistance (bottom) graph comparison over the first 200m of the 1000m wear test.

with forming in the running-in wear regime of metals and ceramics. As there was a stark difference between the running-in wear regime of the Ti64+C and the pure Ti64 conditions, it

was evident that a film developed early into the test from the ceramic addition and contributed to reducing the overall wear of the system. These tribofilms typically hold a higher coefficient of friction from strong bonding with the parent worn surfaces⁴⁸. This observation coincides with this study as the friction coefficient was higher at 0.50 ± 0.01 compared to the 0.32-0.34 in the Ti64 samples. These behaviors led to a reduced overall normalized wear rate of $5.78 \pm 0.12 \times 10^{-5} \text{ mm}^3/\text{N-m}$ in the Ti64+C condition compared to $41.35 \pm 0.45 \times 10^{-5} \text{ mm}^3/\text{N-m}$ in the Ti64 condition compared to $53.17 \pm 0.37 \times 10^{-5} \text{ mm}^3/\text{N-m}$ in the Ti64 substrate.

Design possibilities: To demonstrate these structures' manufacturability even further, gear shapes were produced in multiple states and can be viewed in **Figure 10**. Samples transitioned from a Ti64 composition to the Ti64+C composition with and without a laser pass on the topmost surface. This created a gear shape that has a variation in hardness from the bottom to the

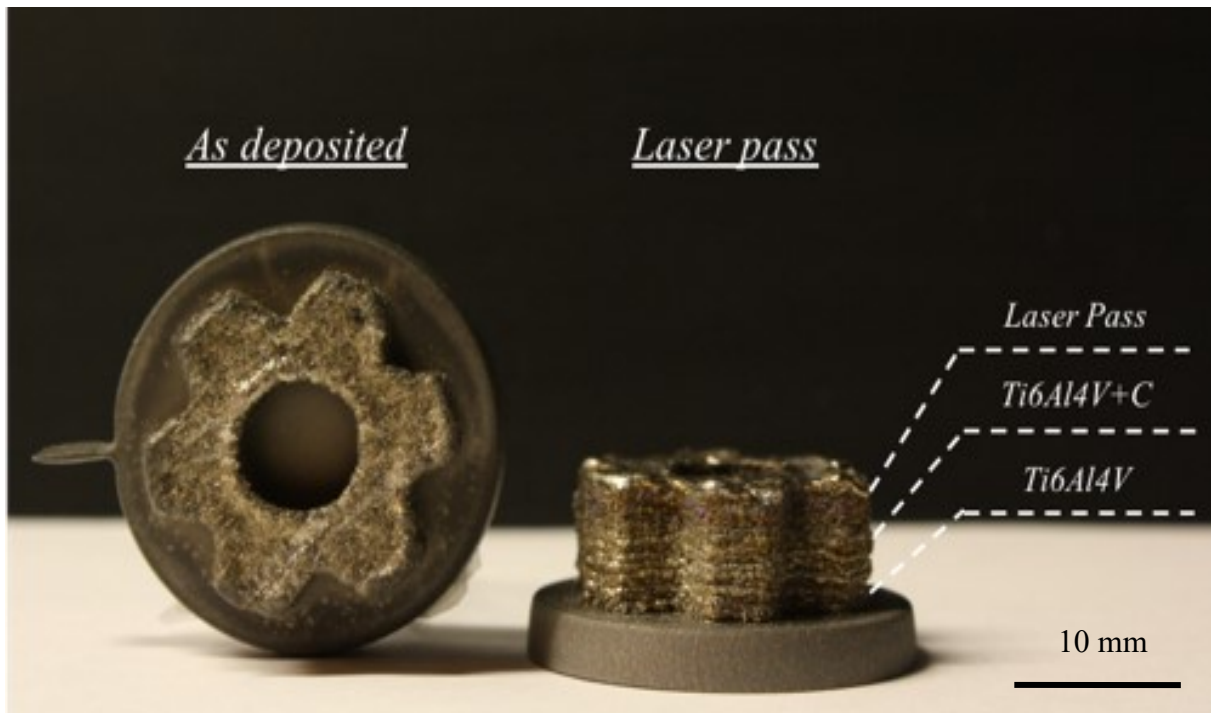


Figure 10: Gear shape transitioning from Ti64 to Ti64+C.

top of the gear structure, and in the laser pass gear, the hardness would be doubled from the bottom of the structure to the top. While this study hopes to impact load-bearing devices for articulating wear, a simple design was used to demonstrate that many structures that could be designed for additive manufacturing, like patient-specific implants, and successfully manufactured with similar tribological enhancements where necessary.

5.0 Conclusions

In this study, functional gradation via LENSTM was coupled with the advantages of Al₂O₃ and SiO₂ to create a composite Ti64 structure with improved hardness and wear resistance. It was hypothesized that with the addition of Al₂O₃ and SiO₂ into Ti64, wear-resistance and hardness would increase when compared to the base Ti64 alloy. It was also hypothesized that if the structure could be created, an additional laser pass (LP) over the structure's top surface would further increase hardness. Successfully fabricated composite structures were found to have varying phases of TiSi₂ and Ti₅Si₃. Refined α -Ti grains were present in the composite region, and the interface between the composite and pure Ti64 regions was crack-free, indicating a metallurgically solid bond. Dendritic microstructures were also observed with the addition of LP on the composite top surface. Hardness was increased from 323.8 ± 9.6 HV in Ti64 substrate to 434.7 ± 7.3 HV and 677.1 ± 29.7 HV in LENSTM-deposited Ti64 and the composite sample, respectively. The addition of an LP increased hardness further to 938.8 ± 57.5 HV, a 186% increase in hardness compared to the original Ti64 alloy. Wear resistance was also increased with the addition of Al₂O₃ and SiO₂ by ~90%, indicating the potential processing variations placed on this material system to produce biomedical structures with site-specific functionality.

6.0 Acknowledgments

The authors would like to acknowledge Michael Kindle from the Nuclear, Optical, Magnetic, and Electronic (NOME) Materials Laboratory at Washington State University and Tom Williams from the Department of Geological Sciences at University of Idaho for XRD analysis and financial support from the National Science Foundation under the grant numbers NSF-CMMI 1538851 (PI - Bandyopadhyay) and NSF-CMMI 1934230 (PI - Bandyopadhyay).

7.0 Conflict of interest: None.

8.0 Data availability statement: Most of the relevant data to reproduce these findings have already been shared in the manuscript. The remaining raw/processed data required to reproduce these findings cannot be shared at this time as the data also forms part of an ongoing study.

9.0 References

- (1) Sansone, V.; Pagani, D.; Melato, M. The Effects on Bone Cells of Metal Ions Released from Orthopaedic Implants. A Review. *Clinical Cases in Mineral and Bone Metabolism*. **2013**, pp 34–40. <https://doi.org/10.11138/ccmbm/2013.10.1.034>.
- (2) Levašič, V.; Milošev, I.; Zadnik, V. Risk of Cancer after Primary Total Hip Replacement: The Influence of Bearings, Cementation and the Material of the Stem: A Retrospective Cohort Study of 8,343 Patients with 9 Years Average Follow-up from Valdoltra Orthopaedic Hospital, Slovenia (*Acta Orth. Acta Orthop*. **2018**, 89 (2), 252. <https://doi.org/10.1080/17453674.2018.1440456>.
- (3) Visuri, T.; Koskenvuo, M. Cancer Risk after McKee-Farrar Total Hip Replacement. *Orthopedics* **1991**, 14 (2), 137–142. <https://doi.org/10.3928/0147-7447-19910201-07>.
- (4) Posada, O. M.; Tate, R. J.; Dominic Meek, R. M.; Helen Grant, M. In Vitro Analyses of the Toxicity, Immunological, and Gene Expression Effects of Cobalt-Chromium Alloy Wear Debris and Co Ions Derived from Metal-on-Metal Hip Implants. *Lubricants*. **2015**, pp 539–568. <https://doi.org/10.3390/lubricants3030539>.

- (5) Berry, D. J. Introduction: The "New" Disease: Taper Corrosion After Total Hip Arthroplasty—A State-of-the-Art Update. *Journal of Arthroplasty*. **2018**, pp 2705–2706. <https://doi.org/10.1016/j.arth.2018.07.008>.
- (6) Pourzal, R.; Lundberg, H. J.; Hall, D. J.; Jacobs, J. J. What Factors Drive Taper Corrosion? *J. Arthroplasty* **2018**, *33* (9), 2707–2711. <https://doi.org/10.1016/j.arth.2018.03.055>.
- (7) Della Valle, C. J.; Calkins, T. E.; Jacobs, J. J. Diagnosing Taper Corrosion: When Is It the Taper and When Is It Something Else? *J. Arthroplasty* **2018**, *33* (9), 2712–2715. <https://doi.org/10.1016/j.arth.2018.01.054>.
- (8) Bolognesi, M. P. Management of the Implant With Taper Corrosion: What to Change and What to Change It To? *J. Arthroplasty* **2018**, *33* (9), 2716–2719. <https://doi.org/10.1016/j.arth.2018.06.016>.
- (9) Mabry, T. M. Preventing Complications Associated With Operating on Taper Corrosion. *J. Arthroplasty* **2018**, *33* (9), 2720–2721. <https://doi.org/10.1016/j.arth.2018.05.033>.
- (10) Fisher, J.; Hu, X. Q.; Stewart, T. D.; Williams, S.; Tipper, J. L.; Ingham, E.; Stone, M. H.; Davies, C.; Hatto, P.; Bolton, J.; Riley, M.; Hardaker, C.; Isaac, G. H.; Berry, G. Wear of Surface Engineered Metal-on-Metal Hip Prostheses. *J. Mater. Sci. Mater. Med.* **2004**, *15* (3), 225–235. <https://doi.org/10.1023/B:JMSM.0000015482.24542.76>.
- (11) Dittrick, S.; Balla, V. K.; Davies, N. M.; Bose, S.; Bandyopadhyay, A. In Vitro Wear Rate and Co Ion Release of Compositionally and Structurally Graded CoCrMo-Ti6Al4V Structures. *Mater. Sci. Eng. C* **2011**, *31* (4), 809–814. <https://doi.org/10.1016/j.msec.2010.07.009>.
- (12) Chen, H.; Xu, C.; Qu, J.; Hutchings, I. M.; Shipway, P. H.; Liu, J. Sliding Wear Behaviour of Laser Clad Coatings Based upon a Nickel-Based Self-Fluxing Alloy Co-Deposited with Conventional and Nanostructured Tungsten Carbide-Cobalt Hardmetals. *Wear* **2005**, *259* (7–12), 801–806. <https://doi.org/10.1016/j.wear.2005.02.066>.
- (13) Tiainen, V. M. Amorphous Carbon as a Bio-Mechanical Coating-Mechanical Properties and Biological Applications. *Diam. Relat. Mater.* **2001**, *10* (2), 153–160. [https://doi.org/10.1016/S0925-9635\(00\)00462-3](https://doi.org/10.1016/S0925-9635(00)00462-3).
- (14) Escobedo, J. C.; Ortiz, J. C.; Almanza, J. M.; Cortés, D. A. Hydroxyapatite Coating on a Cobalt Base Alloy by Investment Casting. *Scr. Mater.* **2006**, *54* (9), 1611–1615. <https://doi.org/10.1016/j.scriptamat.2005.12.059>.
- (15) Piconi, C.; Condo, S. G.; Kosmač, T. Alumina- and Zirconia-Based Ceramics for Load-Bearing Applications. In *Advanced Ceramics for Dentistry*; **2014**; pp 219–253. <https://doi.org/10.1016/B978-0-12-394619-5.00011-0>.

- (16) Zhang, Y.; Bandyopadhyay, A. Direct Fabrication of Compositionally Graded Ti-Al₂O₃ Multi-Material Structures Using Laser Engineered Net Shaping. *Addit. Manuf.* **2018**, *21*, 104–111. <https://doi.org/10.1016/j.addma.2018.03.001>.
- (17) Niu, F.; Wu, D.; Zhou, S.; Ma, G. Power Prediction for Laser Engineered Net Shaping of Al₂O₃ Ceramic Parts. *J. Eur. Ceram. Soc.* **2014**, *34* (15), 3811–3817. <https://doi.org/10.1016/j.jeurceramsoc.2014.06.023>.
- (18) Schwentenwein, M.; Homa, J. Additive Manufacturing of Dense Alumina Ceramics. *Int. J. Appl. Ceram. Technol.* **2015**, *12* (1), 1–7. <https://doi.org/10.1111/ijac.12319>.
- (19) Li, Y.; Hu, Y.; Cong, W.; Zhi, L.; Guo, Z. Additive Manufacturing of Alumina Using Laser Engineered Net Shaping: Effects of Deposition Variables. *Ceram. Int.* **2017**, *43* (10), 7768–7775. <https://doi.org/10.1016/j.ceramint.2017.03.085>.
- (20) Hu, Y.; Ning, F.; Cong, W.; Li, Y.; Wang, X.; Wang, H. Ultrasonic Vibration-Assisted Laser Engineering Net Shaping of ZrO₂-Al₂O₃ Bulk Parts: Effects on Crack Suppression, Microstructure, and Mechanical Properties. *Ceram. Int.* **2018**, *44* (3), 2752–2760. <https://doi.org/10.1016/j.ceramint.2017.11.013>.
- (21) Niu, F.; Wu, D.; Ma, G.; Wang, J.; Zhuang, J.; Jin, Z. Rapid Fabrication of Eutectic Ceramic Structures by Laser Engineered Net Shaping. In *Procedia CIRP*; **2016**; Vol. 42, pp 91–95. <https://doi.org/10.1016/j.procir.2016.02.196>.
- (22) Migaud, H.; Putman, S.; Kern, G.; Isida, R.; Girard, J.; Ramdane, N.; Delaunay, C. P.; Hamadouche, M.; The SoFCOT Study Group. Do the Reasons for Ceramic-on-Ceramic Revisions Differ From Other Bearings in Total Hip Arthroplasty? *Clin. Orthop. Relat. Res.* **2016**, *474* (10), 2190–2199. <https://doi.org/10.1007/s11999-016-4917-x>.
- (23) Schneider, H.; Schreuer, J.; Hildmann, B. Structure and Properties of Mullite-A Review. *J. Eur. Ceram. Soc.* **2008**, *28* (2), 329–344. <https://doi.org/10.1016/j.jeurceramsoc.2007.03.017>.
- (24) Heer, B.; Bandyopadhyay, A. Silica Coated Titanium Using Laser Engineered Net Shaping for Enhanced Wear Resistance. *Addit. Manuf.* **2018**, *23*, 303–311. <https://doi.org/10.1016/j.addma.2018.08.022>.
- (25) Jiménez, A. E.; Morina, A.; Neville, A.; Bermúdez, M. D. Surface Interactions and Tribochemistry in Boundary Lubrication of Hypereutectic Aluminium-Silicon Alloys. *Proc. Inst. Mech. Eng. Part J J. Eng. Tribol.* **2009**, *223* (3), 593–601. <https://doi.org/10.1243/13506501JET528>.
- (26) Gao, C. P.; Guo, G. F.; Zhao, F. Y.; Wang, T. M.; Jim, B.; Wetzel, B.; Zhang, G.; Wang, Q. H. Tribological Behaviors of Epoxy Composites under Water Lubrication Conditions. *Tribol. Int.* **2016**, *95*, 333–341. <https://doi.org/10.1016/j.triboint.2015.11.041>.

- (27) Vamsi Krishna, B.; Xue, W.; Bose, S.; Bandyopadhyay, A. Functionally Graded Co-Cr-Mo Coating on Ti-6Al-4V Alloy Structures. *Acta Biomater.* **2008**, *4* (3), 697–706. <https://doi.org/10.1016/j.actbio.2007.10.005>.
- (28) Sahasrabudhe, H.; Soderlind, J.; Bandyopadhyay, A. Laser Processing of in Situ TiN/Ti Composite Coating on Titanium. *J. Mech. Behav. Biomed. Mater.* **2016**, *53*, 239–249. <https://doi.org/10.1016/j.jmbbm.2015.08.013>.
- (29) Li, J.; Yu, Z.; Wang, H. Wear Behaviors of an (TiB + TiC)/Ti Composite Coating Fabricated on Ti6Al4V by Laser Cladding. In *Thin Solid Films*; **2011**; Vol. 519, pp 4804–4808. <https://doi.org/10.1016/j.tsf.2011.01.034>.
- (30) Mahamood, R. M.; Akinlabi, E. T.; Shukla, M.; Pityana, S. Scanning Velocity Influence on Microstructure, Microhardness and Wear Resistance Performance of Laser Deposited Ti6Al4V/TiC Composite. *Mater. Des.* **2013**, *50*, 656–666. <https://doi.org/10.1016/j.matdes.2013.03.049>.
- (31) Liu, W.; DuPont, J. N. Fabrication of Functionally Graded TiC/Ti Composites by Laser Engineered Net Shaping. *Scr. Mater.* **2003**, *48* (9), 1337–1342. [https://doi.org/10.1016/S1359-6462\(03\)00020-4](https://doi.org/10.1016/S1359-6462(03)00020-4).
- (32) Liu, S.; Shin, Y. C. The Influences of Melting Degree of TiC Reinforcements on Microstructure and Mechanical Properties of Laser Direct Deposited Ti6Al4V-TiC Composites. *Mater. Des.* **2017**, *136*, 185–195. <https://doi.org/10.1016/j.matdes.2017.09.063>.
- (33) Mahamood, R. M.; Akinlabi, E. T. Laser Metal Deposition of Functionally Graded Ti6Al4V/TiC. *Mater. Des.* **2015**, *84*, 402–410. <https://doi.org/10.1016/j.matdes.2015.06.135>.
- (34) Das, M.; Balla, V. K.; Basu, D.; Manna, I.; Sampath Kumar, T. S.; Bandyopadhyay, A. Laser Processing of in Situ Synthesized TiB-TiN-Reinforced Ti6Al4V Alloy Coatings. *Scr. Mater.* **2012**, *66* (8), 578–581. <https://doi.org/10.1016/j.scriptamat.2012.01.010>.
- (35) Das, M.; Bysakh, S.; Basu, D.; Sampath Kumar, T. S.; Balla, V. K.; Bose, S.; Bandyopadhyay, A. Microstructure, Mechanical and Wear Properties of Laser Processed SiC Particle Reinforced Coatings on Titanium. *Surf. Coatings Technol.* **2011**, *205* (19), 4366–4373. <https://doi.org/10.1016/j.surfcoat.2011.03.027>.
- (36) ASTM International. G133-05 Linearly Reciprocating Ball-on-Flat Sliding Wear. *ASTM Int.* **2016**, *i* (Reapproved 2016), 1–9.
- (37) Kirka, M. M.; Nandwana, P.; Lee, Y.; Dehoff, R. R. Solidification and Solid-State Transformation Sciences in Metals Additive Manufacturing. *Scr. Mater.* **2017**, *135*, 130–134. <https://doi.org/10.1016/j.scriptamat.2017.01.005>.

- (38) Thijs, L.; Verhaeghe, F.; Craeghs, T.; Humbeeck, J. Van; Kruth, J. P. A Study of the Microstructural Evolution during Selective Laser Melting of Ti-6Al-4V. *Acta Mater.* **2010**. <https://doi.org/10.1016/j.actamat.2010.02.004>.
- (39) Wang, T.; Zhu, Y. Y.; Zhang, S. Q.; Tang, H. B.; Wang, H. M. Grain Morphology Evolution Behavior of Titanium Alloy Components during Laser Melting Deposition Additive Manufacturing. *J. Alloys Compd.* **2015**, *632*, 505–513. <https://doi.org/10.1016/j.jallcom.2015.01.256>.
- (40) Saboori, A.; Gallo, D.; Biamino, S.; Fino, P.; Lombardi, M. An Overview of Additive Manufacturing of Titanium Components by Directed Energy Deposition: Microstructure and Mechanical Properties. *Applied Sciences (Switzerland)*. **2017**. <https://doi.org/10.3390/app7090883>.
- (41) Donachie, M. J. Understanding the Metallurgy of Titanium, in: Titan. A Tech. Guid. 2nd Ed., *ASM International*, **2000**: p. 16. <https://books.google.com/books?id=HgzukknbNGAC>.
- (42) Ahmed, T.; Rack, H. J. Phase Transformations during Cooling in $\alpha + \beta$ Titanium Alloys. *Mater. Sci. Eng. A* **1998**, *243* (1–2), 206–211. [https://doi.org/10.1016/s0921-5093\(97\)00802-2](https://doi.org/10.1016/s0921-5093(97)00802-2).
- (43) Gammon L.M.; Briggs R.D.; Packard J.M.; Batson K.W.; Boyer R.; Dombay C.W.; Metallography and Microstructures of Titanium and its Alloys, in: G.F. Vander Voort (Ed.), *ASM Handbook*, Vol. 9 Metallogr. Microstruct., **2004**: pp. 899–917. doi:10.1361/asmhba0003779.
- (44) Schlesinger, M. E. Thermodynamics of Solid Transition-Metal Silicides. *Chem. Rev.* **1990**, *90* (4), 607–628. <https://doi.org/10.1021/cr00102a003>.
- (45) Trambukis, J.; Munir, Z. A. Effect of Particle Dispersion on the Mechanism of Combustion Synthesis of Titanium Silicide. *J. Am. Ceram. Soc.* **1990**, *73* (5), 1240–1245. <https://doi.org/10.1111/j.1151-2916.1990.tb05186.x>.
- (46) Bandyopadhyay, A.; Dittrick, S.; Gualtieri, T.; Wu, J.; Bose, S. Calcium Phosphate-Titanium Composites for Articulating Surfaces of Load-Bearing Implants. *J. Mech. Behav. Biomed. Mater.* **2016**, *57*, 280–288. <https://doi.org/10.1016/j.jmbbm.2015.11.022>.
- (47) American Society for Testing and Materials. *ASTM Standard G40-15: Standard Terminology Relating to Wear and Erosion*; **2015**.
- (48) Luo, Q. Tribofilms in Solid Lubricants. In *Encyclopedia of Tribology*; **2013**; pp 3760–3767. https://doi.org/10.1007/978-0-387-92897-5_1252.
- (49) Dowson, D.; Hardaker, C.; Flett, M.; Isaac, G. H. A Hip Joint Simulator Study of the Performance of Metal-on-Metal Joints: Part I: The Role of Materials. In *Journal of*

Arthroplasty; **2004**; Vol. 19, pp 118–123. <https://doi.org/10.1016/j.arth.2004.09.015>.